Journal of Materials Science and Chemical Engineering, 2025, 13(11), 79-88
https://www.scirp.org/journal/msce
ISSN Online: 2327-6053
ISSN Print: 2327-6045

Modification of Transition Metal Catalysts and Their Application in the Oxygen Reduction Reaction

Sunxuan Lu

Jiangsu Normal University, Xuzhou, China
Email: 2928380389@qq.com

How to cite this paper: Lu, S.X. (2025) Modification of Transition Metal Catalysts and Their Application in the Oxygen Reduction Reaction. *Journal of Materials Science and Chemical Engineering*, **13**, 79-88.
https://doi.org/10.4236/msce.2025.1311006

Received: October 31, 2025
Accepted: November 24, 2025
Published: November 27, 2025

Abstract

Fuel cells, as a novel energy source, have garnered widespread attention due to their high efficiency, environmental friendliness, and exceptional reliability. The oxygen reduction reaction (ORR) serves as the critical cathode reaction in fuel cells, whose sluggish kinetics necessitate the use of highly efficient catalysts. To date, platinum (Pt)-based materials exhibit the highest ORR performance, establishing themselves as commercial catalysts for fuel cells. However, Pt's high cost, limited resources, and poor thermal stability have driven research into efficient non-precious metal catalysts. Transition metal-nitrogen-carbon (M-N-C) catalysts have emerged as promising alternatives due to their stability, high surface area, excellent conductivity, and low manufacturing costs. Among these, Fe-N-C catalysts have garnered significant attention for exhibiting Pt-like activity in ORR. However, issues such as low loading and utilization of Fe-N_4 active sites and inherently low intrinsic activity in Fe-N-C catalysts have prevented their catalytic performance from reaching an ideal state. To enhance the ORR performance of Fe-N-C catalysts, it is essential to select an appropriate carbon support to anchor a large number of iron (Fe) single atoms and to regulate the electronic structure of Fe-N_4 sites through targeted defect engineering, thereby improving the intrinsic activity of Fe-N_4 active sites. This work employs three-dimensional ZIF-8 as a precursor, iron nitrate as the Fe source, and utilizes urea etching to synthesize the single-atom Fe-N-C-2 catalyst in a one-step process. Numerous Fe atoms are uniformly distributed on the porous carbon framework with a dodecahedral structure, significantly increasing the loading and utilization of Fe-N_4 active sites. Simultaneously, urea etching selectively breaks C-N bonds adjacent to Fe-N_4 active centers, creating carbon vacancies and disrupting the symmetry of the Fe-N_4 local electronic structure, thereby enhancing its intrinsic activity. Consequently, the Fe-N-C-2 catalyst exhibits outstanding ORR activity in acidic

electrolytes, achieving an $E_{1/2}$ value of 0.934 V in acidic media, along with excellent environmental durability and cycling stability.

Keywords

Transition Metal Catalysts, Oxygen Reduction, Overpotential

1. Introduction

As global energy demand continues to rise and environmental issues stemming from excessive fossil fuel exploitation intensify, developing an efficient clean energy system is the only viable solution to this problem and an effective pathway for China to achieve its dual carbon goals. Although renewable energy sources like solar and wind power play a significant role, their energy storage bottlenecks and intermittent supply severely limit large-scale application [1]-[3]. In contrast, hydrogen energy, with its ultra-high calorific value, long-term energy storage capabilities, and core advantage of zero-carbon emissions at the end-use stage, has emerged as a strategic choice for building a new energy system. Current mainstream hydrogen production technologies include fossil fuel reforming, biohydrogenation, photolysis, and water electrolysis. Among these, water electrolysis is regarded as the ultimate solution for green hydrogen production due to its advantages: product purity exceeding 99.99%, zero carbon emissions throughout the process, and a simple process. However, this technology faces two major bottlenecks: first, slow reaction kinetics requiring high overpotentials to drive water's redox reactions [4]-[7]; second, reliance on precious metal catalysts (e.g., Pt, Ir, Ru) to lower the reaction energy barrier. Precious metals are scarce on Earth's surface and prohibitively expensive, severely limiting large-scale application.

Addressing these challenges, there is an urgent need to develop transition metal catalytic materials to replace precious metals. Since metal catalysts exhibit optimal performance at the atomic dispersion level, the limited dispersion of active sites in traditional transition metal catalysts restricts catalytic efficiency. Utilizing zeolite imidazolium frameworks (ZIFs) can anchor metal atoms, enabling atomic-level dispersion. As early as 2011, the research team led by Academician Zhang Tao of the Chinese Academy of Sciences proposed the concept of "Single-Atom Catalysis" (SAC). Single-atom platinum catalysts prepared using ZIF [8]-[10] demonstrated exceptionally high catalytic activity and stability, becoming a popular research direction. However, the isolated active sites in SAC often lead to issues such as strong adsorption of intermediates and limited electron transfer pathways, restricting its application scope. To address this, this study employed a solvothermal method to prepare dual-atom catalysts (DAC). By designing synergistic effects between two metal atoms, the performance bottlenecks of single-atom catalysts were overcome. The dual-atom catalyst significantly enhances catalytic activity and stability through mechanisms such as electron coupling, geometric

steric hindrance regulation, and synergistic adsorption, offering a novel strategy to overcome the kinetic bottleneck in water electrolysis for hydrogen production.

2. Material Preparation

2.1. Preparation of ZIF-8

Here, 2.628 g of 2-methylimidazole and 1.188 g of zinc nitrate were added to 50 mL of methanol solution and stirred at room temperature until completely dissolved. The mixture was stirred at room temperature for 24 h. The precipitate was collected by centrifugation and washed several times with methanol until the supernatant became clear. Finally, the prepared product was vacuum-dried overnight at 60˚C prior to use. ZIF-8 with a particle size of 40 nm was obtained.

2.2. Preparation of Fe-ZIF-8

Add 2.628 g of 2-methylimidazole, 1.188 g of zinc nitrate, and 0.35 g of ferrocene to 50 mL of methanol solution. Stir at room temperature until completely dissolved, then continue stirring for 24 hours. The precipitate was collected by centrifugation and washed several times with methanol until the supernatant became clear. Finally, the prepared product was vacuum-dried overnight at 60˚C prior to use.

2.3. Preparation of Fe-N-C-x

Add 2.628 g of 2-methylimidazole, 1.188 g of zinc nitrate, and 0.35 g of ferrocene to 50 mL of methanol solution. During synthesis, urea was added at varying concentrations. Samples corresponding to molar ratios of ferrocene to urea of (1:0.15, 1:0.8, 1:1.5, 1:4, 1:8) yielded samples designated Fe-ZIF-8-1, Fe-ZIF-8-2, Fe-ZIF-8-3, Fe-ZIF-8-4, and Fe-ZIF-8-5, respectively. The mixture was stirred at room temperature until complete dissolution, followed by continued stirring for 24 h. The precipitate was collected by centrifugation and washed several times with methanol until the supernatant became clear. Finally, the prepared product was vacuum-dried overnight at 60˚C prior to use. Fe-ZIF-8 was heated at 5˚C/min to 900˚C under an Ar atmosphere, held for 3 h to yield Fe-N-C-O samples. Fe-ZIF-8-x (Fe-ZIF-8-1, Fe-ZIF-8-2, Fe-ZIF-8-3, Fe-ZIF-8-4, and Fe-ZIF-8-5) were heated at 5˚C/min to 900˚C under an Ar atmosphere and held at 900˚C for 3 h to obtain Fe-N-C-x samples (Fe-N-C-1, Fe-N-C-2, Fe-N-C-3, Fe-N-C-4, and Fe-N-C-5).

3. Results and Discussion

Figure 1 illustrates the schematic synthesis strategy for Fe-N-C-x materials. This process utilizes ZIF-8 as a precursor, achieving Fe doping by introducing an iron source to form FeZIF-8 composite materials. During subsequent thermal activation treatment, some Zn atoms are replaced by Fe atoms, ultimately forming a hierarchical porous carbon framework with abundant defects and high nitrogen doping levels—the Fe-N-C-0 material. To further modulate the material structure,

urea is incorporated at varying ratios as a modifier during synthesis. During pyrolysis [11], urea decomposes to release ammonia gas, which etches the ZIF-8-derived carbon carrier, introducing vacancy defects. This etching process promotes selective cleavage of C-N bonds adjacent to Fe-N_4 sites, altering the local charge density distribution and electronic structure around the Fe-N_4 center. This results in the formation of Fe-N_4 active sites with pronounced charge asymmetry. This electronic restructuring significantly reduces the free energy barrier for the oxygen reduction reaction (ORR), effectively enhancing the electrocatalytic ORR process.

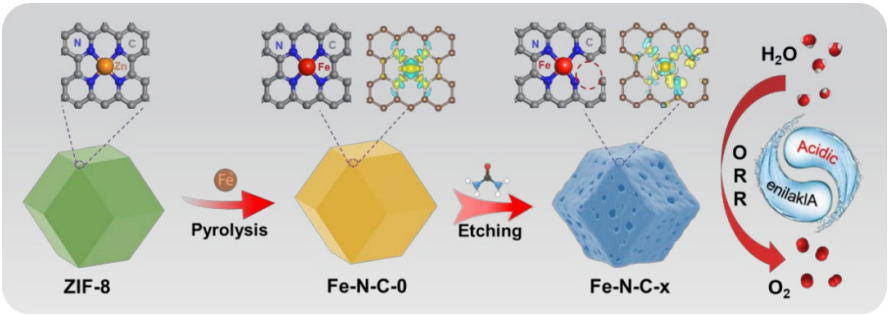

Figure 1. Schematic of the synthesis strategy for Fe-N-C-x materials

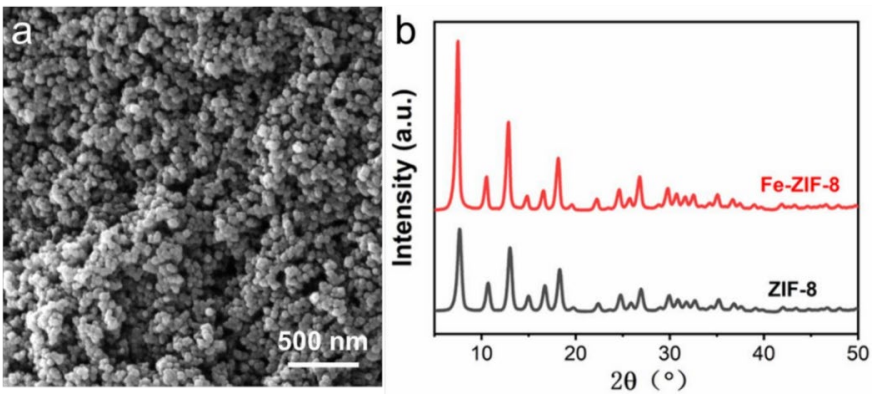

Figure 2. (a) SEM image of Fe-ZIF-8 (b) XRD patterns of Fe-ZIF-8 and ZIF-8.

Figure 2(a) shows the SEM image of Fe-ZIF-8. The image reveals that Fe-ZIF-8 consists of numerous uniformly sized nanoparticles. These particles aggregate to form a relatively loose structure, with particle sizes around tens of nanometers. This nanoscale morphology enhances the material's specific surface area, providing more active sites for adsorption, catalysis, and other processes. The XRD patterns of Fe-ZIF-8 and ZIF-8 are shown in **Figure 2(b)**. The diffraction peak positions of Fe-ZIF-8 are essentially consistent with those of ZIF-8, indicating that Fe doping has not altered the fundamental crystal structure of ZIF-8. This confirms the successful incorporation of Fe into the ZIF-8 framework, resulting in Fe-ZIF-8 with a similar crystal structure. Concurrently, the diffraction peak intensities of Fe-ZIF-8 exhibit enhanced values, potentially attributable to increased crystallinity following Fe doping. This enhancement may relate to the promoting effect of Fe

ions on crystal growth during the synthesis process.

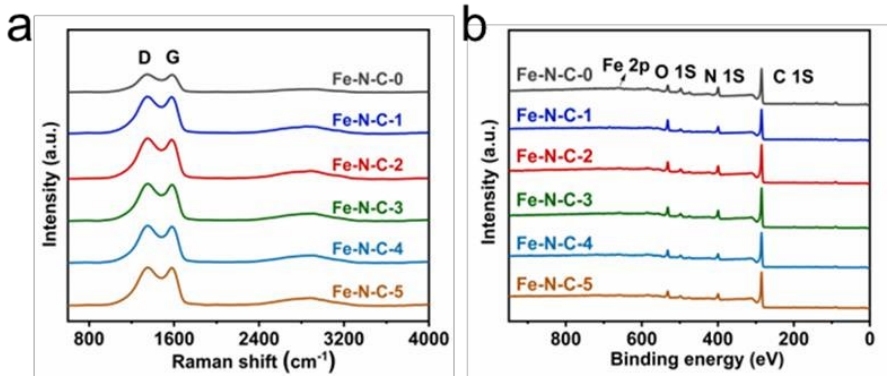

Figure 3. (a) Raman spectrum of the catalyst (b) Full XPS spectrum.

Raman spectroscopy was performed to evaluate the defect level of carbon in the material, as shown in **Figure 3**. Two broad main peaks were observed at 1352 cm^{-1} and 1572 cm^{-1}, corresponding to the D and G bands of carbon, respectively. It is widely recognized that the relative intensity ratio (ID/IG) of the D and G bands provides evidence for the degree of graphitization and defect content in carbon. The results show that the ID/IG values for Fe-N-C-0, Fe-N-C-1, Fe-N-C-2, Fe-N-C-3, Fe-N-C-4, and Fe-N-C-5 exhibit ID/IG values of 0.98, 1.01, 1.03, 1.05, and 1.08, respectively. This indicates that urea addition produces a pronounced etching effect on the carbon material, increasing the defect density of the Fe-N-C-x catalysts. We propose that the carbon vacancy content should be proportional to the degree of asymmetry. Fe-N-C-2 exhibits a moderate specific surface area with high microporosity, corresponding to the highest ID/IG value in the Raman spectrum. While excessive etching may further increase specific surface area and carbon vacancy density, it leads to structural collapse of the carbon material, hindering further performance enhancement. Subsequently, XPS characterization was employed to investigate the surface composition of the synthesized catalysts.

The detailed XPS spectrum is shown in **Figure 4**. All Fe-N-C-x samples are dominated by C, N, O, and Fe elements, confirming the successful preparation of the materials. The high-resolution C 1s spectra of all samples can be fitted to three characteristic peaks at 284.8 eV, 286.0 eV, and 288.3 eV, representing C-C, C-N, and C=O bonds, respectively (**Figure 4**). The C-N bond content in Fe-N-C-x samples decreased with urea addition, attributed to urea's etching effect that disrupted C-N bonds adjacent to Fe-N_4 phases, indicating selective cleavage of C-N bonds. LSV test results (**Figure 5(a)**) show that Fe-N-C-0 exhibits an $E_{1/2}$ of 0.862 V in 0.1 M $HClO_4$. This may be attributed to the small size (40 nm) of the synthesized ZIF-8, which possesses a large number of active sites per unit area.

The addition of urea during synthesis further enhances the ORR catalytic activity of the Fe-N-C-x catalyst. As the urea content increases, the $E_{1/2}$ value of the samples undergoes an initial rise followed by a gradual decrease. Notably, Fe-N-C-2 exhibits the highest activity among the Fe-N-C-x catalysts, featuring an

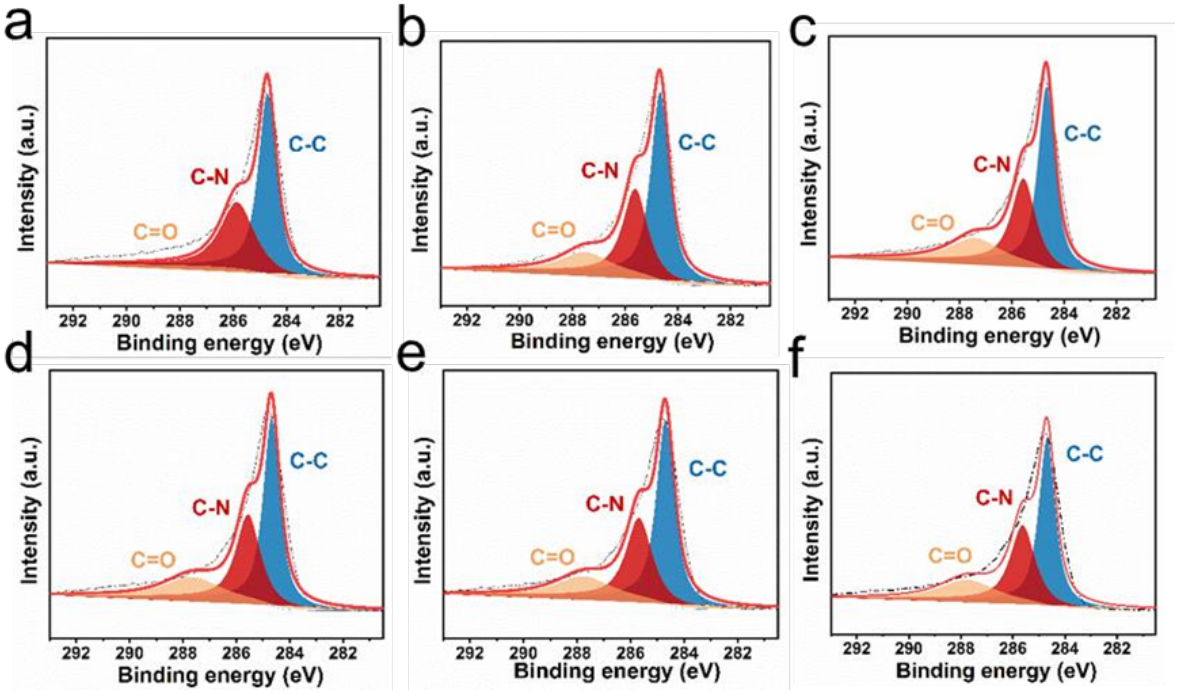

Figure 4. Detailed XPS Spectrum.

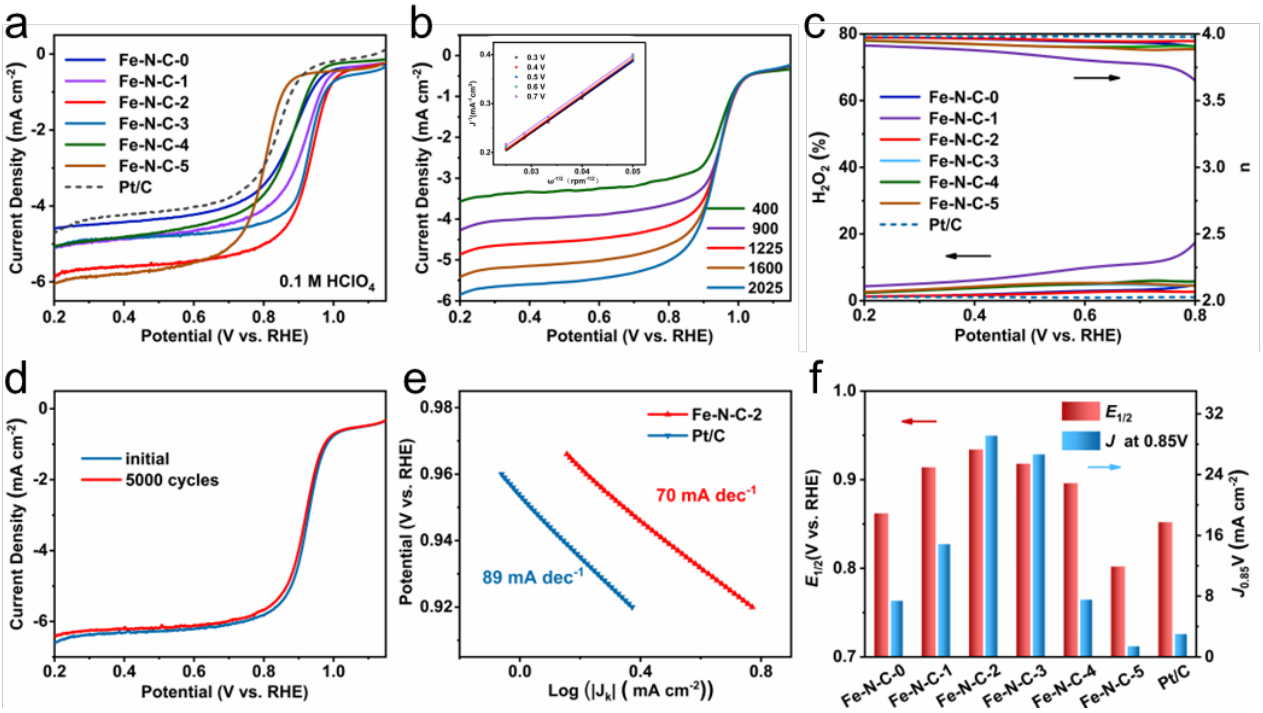

Figure 5. (a) LSV test curve of the catalyst (b) LSV tests at different rotational speeds (c) RRDE test (d) LSV test after 5000 cycles (e) Tafel slope (f) Summary bar chart of data.

E_(onset) of 1.015 V and an $E_{1/2}$ of 0.934 V—both significantly higher than commercial Pt/C (Eonset) = 1.002 V, $E_{1/2}$ = 0.862 V) and previously reported non-precious metal catalysts. The enhanced ORR performance is attributed to the

synergistic effects of the ultramicroscopic carbon framework with large specific surface area and defect engineering. Specifically, urea-controlled defects further increase the specific surface area and induce abundant three-dimensional porous structures within the carbon framework, providing sufficient loading sites for Fe-N_4. Additionally, the defect-rich nature of the carbon framework facilitates mass diffusion and electron transfer during the electrocatalytic process. However, excessive urea addition (e.g., Fe-N-C-3, Fe-N-C-4, and Fe-N-C-5) severely disrupts the dodecahedral structure, reducing exposed active sites and consequently diminishing ORR catalytic activity. Thus, optimal catalytic performance is achieved by tuning the urea doping amount. **Figure 5(b)** shows the LSV curves of Fe-N-C-2, which exhibits the highest ORR catalytic activity, at different scan rates, along with the calculated K-L curves. The results indicate that the electron transfer number (n) for Fe-N-C-2 exceeds 3.91 within the 0.3–0.7 V range, confirming a four-electron reaction mechanism for the ORR on Fe-N-C-2 in 0.1 M $HClO_4$. The selectivity toward hydroxide formation is close to that of the four-electron pathway. To further validate selectivity, ring current and disc current were measured using a rotating ring-disk electrode (RRDE) in 0.1 M $HClO_4$, and the catalyst's H_2O_2 yield was fitted (**Figure 5(c)**). Fe-N-C-2 exhibited extremely low H_2O_2 yield between potentials of 0.2 V and 0.8 V. Following LSV testing of Fe-N-C-2, stability testing was conducted. The electrolyte was saturated with N_2 by re-injecting N_2 into the 0.1 M $HClO_4$ solution. Cyclic voltammetry was performed at 900 rpm for 5000 cycles. Subsequently, O_2 was introduced to saturate the 0.1 M $HClO_4$ electrolyte with O_2. The LSV profile was measured using RDE at 1600 rpm. as shown in **Figure 5(d)**. Comparison with the previously tested LSV curve indicates that the $E_{1/2}$ value of Fe-N-C-2 exhibits negligible negative shift after 5000 cycles, demonstrating excellent durability of this catalyst in acidic solutions. Fitting the LSV profile yielded the Tafel slope plot for Fe-N-C-2 (**Figure 5(e)**). The Tafel slope of Fe-N-C-2 was 70 $mV \cdot dec^{-1}$, lower than that of the Pt/C catalyst (89 $mV \cdot dec^{-1}$), indicating faster electron transfer rates and higher catalytic activity for Fe-N-C-2. Additionally, the current density within the kinetic range of Fe-N-C_2 (J_k = 0.85 V) further demonstrates that this catalyst exhibits significantly higher activity than other materials (**Figure 5(f)**).

Additionally, we employed the current-time (i-t) method to evaluate the ORR lifetime of Fe-N-C-2, as shown in **Figure 6**. The test was conducted at 0.6 V (vs. RHE) with a rotation speed of 900 rpm, plotting the current value versus time. Minimal variation indicates excellent stability of the oxygen reduction catalyst. After 35,000 s of continuous reaction, Fe-N-C-2 exhibited an initial current density retention of 87.3%, while the Pt/C catalyst showed 63.8%, further confirming its outstanding durability [11]. (**Figure 4**). These results demonstrate that the synthesized Fe-N-C-2 catalyst exhibits outstanding ORR catalytic performance under acidic conditions.

4. Conclusions and Outlook

This study successfully developed a single-atom Fe-N-C-2 catalyst synthesized via

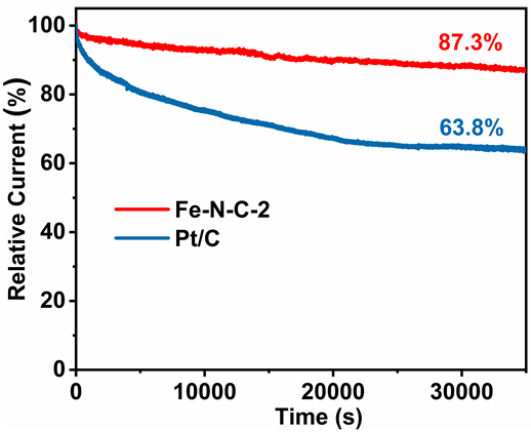

Figure 6. Time-current (i-t) curve for ORR catalyst stability testing.

a urea-assisted defect engineering strategy to enhance catalytic performance for the oxygen reduction reaction in acidic media. Using ZIF-8 as a precursor, this catalyst combines the synergistic effects of iron nitrate and urea to achieve highly dispersed Fe atoms within the carbon framework [12] and high loading of Fe-N_4 active sites during pyrolysis. Urea etching not only introduces abundant carbon vacancies but also disrupts the local electronic symmetry of Fe-N_4 centers, significantly enhancing their intrinsic ORR activity. Experimental results demonstrate that Fe-N-C-2 exhibits outstanding ORR performance in 0.1 M $HClO_4$, with a half-wave potential as high as 0.934 V, surpassing commercial Pt/C catalysts. It also displays high selectivity, low hydrogen peroxide yield, and excellent cycling stability and durability, consistent with a four-electron transfer pathway [13]-[15]. This study provides an effective strategy for regulating the electronic structure of M-N-C catalysts through defect engineering to enhance their catalytic performance.

Although this work successfully prepared high-performance catalysts via a urea-assisted defect engineering strategy, demonstrating outstanding ORR activity and zinc-air battery performance, several critical scientific and technological issues remain to be explored for its ultimate commercialization. First, precise control over active sites and mechanistic understanding require further refinement. While this study confirms the critical role of asymmetric configurations in enhancing intrinsic activity, the exact concentration, distribution, and quantitative influence mechanism of carbon vacancies [10] on the electronic structure of Fe centers remain unclear. Future research should integrate advanced in situ characterization techniques (e.g., *in-situ* X-ray absorption spectroscopy, Mössbauer spectroscopy) with theoretical calculations to establish precise structure-activity relationships linking vacancy structure, electronic states, and catalytic performance, thereby providing theoretical support for targeted active site design. Second, long-term stability under harsh acidic conditions or high current density remains a core bottleneck limiting practical catalyst application. Future work should systematically investigate the evolution of active sites [11]-[14] during long-term

operation, including Fe atom leaching, agglomeration, oxidation corrosion of the carbon support, and deactivation due to H_2O_2 attack. Novel stabilization strategies—such as carbon layer encapsulation, synergistic coordination with heteroatoms (S, P, etc.), or constructing rigid carbon frameworks—hold promise for significantly enhancing catalyst durability. Finally, investigating the universality of this strategy holds considerable research value. Whether this urea etching and defect-building approach can be successfully extended to other transition metals (e.g., Co, Mn) or bimetallic M-N-C systems to regulate their performance in different catalytic reactions (e.g., OER, NRR, CO2RR) represents a promising research direction.

Conflicts of Interest

The author declares no conflicts of interest regarding the publication of this paper.

References

[1] Kovač, A., Paranos, M. and Marciuš, D. (2021) Hydrogen in Energy Transition: A Review. *International Journal of Hydrogen Energy*, **46**, 10016-10035. https://doi.org/10.1016/j.ijhydene.2020.11.256

[2] Zhang, F., Zhao, P., Niu, M. and Maddy, J. (2016) The Survey of Key Technologies in Hydrogen Energy Storage. *International Journal of Hydrogen Energy*, **41**, 14535-14552. https://doi.org/10.1016/j.ijhydene.2016.05.293

[3] Lu, H., Tournet, J., Dastafkan, K., Liu, Y., Ng, Y.H., Karuturi, S.K., *et al.* (2021) Noble-metal-free Multicomponent Nanointegration for Sustainable Energy Conversion. *Chemical Reviews*, **121**, 10271-10366. https://doi.org/10.1021/acs.chemrev.0c01328

[4] Seh, Z.W., Kibsgaard, J., Dickens, C.F., Chorkendorff, I., Nørskov, J.K. and Jaramillo, T.F. (2017) Combining Theory and Experiment in Electrocatalysis: Insights into Materials Design. *Science*, **355**, eaad4998. https://doi.org/10.1126/science.aad4998

[5] El-Shafie, M. (2023) Hydrogen Production by Water Electrolysis Technologies: A Review. *Results in Engineering*, **20**, Article ID: 101426. https://doi.org/10.1016/j.rineng.2023.101426

[6] Sun, H., Xu, X., Kim, H., Jung, W., Zhou, W. and Shao, Z. (2023) Electrochemical Water Splitting: Bridging the Gaps between Fundamental Research and Industrial Applications. *Energy & Environmental Materials*, **6**, e12441. https://doi.org/10.1002/eem2.12441

[7] Peng, O., Shi, R., Wang, J., Zhang, X., Miao, J., Zhang, L., *et al.* (2020) Hierarchical Heterostructured Nickle Foam-Supported Co_3S_4 Nanorod Arrays Embellished with Edge-Exposed MoS_2 Nanoflakes for Enhanced Alkaline Hydrogen Evolution Reaction. *Materials Today Energy*, **18**, Article ID: 100513. https://doi.org/10.1016/j.mtener.2020.100513

[8] Zhang, Z., Jiang, C., Li, P., Yao, K., Zhao, Z., Fan, J., *et al.* (2021) Benchmarking Phases of Ruthenium Dichalcogenides for Electrocatalysis of Hydrogen Evolution: Theoretical and Experimental Insights. *Small*, **17**, Article ID: 2007333. https://doi.org/10.1002/smll.202007333

[9] Wang, C., Humayun, M., Debecker, D.P. and Wu, Y. (2023) Electrocatalytic Water Oxidation with Layered Double Hydroxides Confining Single Atoms. *Coordination Chemistry Reviews*, **478**, Article ID: 214973. https://doi.org/10.1016/j.ccr.2022.214973

[10] Ge, J., Liu, Z., Guan, M., Kuang, J., Xiao, Y., Yang, Y., *et al.* (2022) Investigation of the Electrocatalytic Mechanisms of Urea Oxidation Reaction on the Surface of Transition Metal Oxides. *Journal of Colloid and Interface Science*, **620**, 442-453. https://doi.org/10.1016/j.jcis.2022.03.152

[11] Li, J., Cui, H., Du, X. and Zhang, X. (2022) The Controlled Synthesis of Nitrogen and Iron Co-Doped Ni_3S_2@NiP_2 Heterostructures for the Oxygen Evolution Reaction and Urea Oxidation Reaction. *Dalton Transactions*, **51**, 2444-2451. https://doi.org/10.1039/d1dt03933d

[12] Zouhri, K. and Lee, S. (2016) Evaluation and Optimization of the Alkaline Water Electrolysis Ohmic Polarization: Exergy Study. *International Journal of Hydrogen Energy*, **41**, 7253-7263. https://doi.org/10.1016/j.ijhydene.2016.03.119

[13] Navarro-Flores, E., Chong, Z. and Omanovic, S. (2005) Characterization of Ni, NiMo, NiW and NiFe Electroactive Coatings as Electrocatalysts for Hydrogen Evolution in an Acidic Medium. *Journal of Molecular Catalysis A*: *Chemical*, **226**, 179-197. https://doi.org/10.1016/j.molcata.2004.10.029

[14] Wang, Z., Hu, Y., Liu, W., Xu, L., Guan, M., Zhao, Y., *et al.* (2020) Manganese-Modulated Cobalt-Based Layered Double Hydroxide Grown on Nickel Foam with 1D-2D-3D Heterostructure for Highly Efficient Oxygen Evolution Reaction and Urea Oxidation Reaction. *Chemistry—A European Journal*, **26**, 9382-9388. https://doi.org/10.1002/chem.202001055

[15] Zou, J. and Ren, X. (2023) A Computational Study of Design and Performance Investigation of Ni-Based Electrocatalysts for Efficient Electrocatalytic Hydrogen Evolution Reaction. *New Journal of Chemistry*, **47**, 14408-14417. https://doi.org/10.1039/d3nj02351f